

Supplementary Information for Temperature-responsive multistable metamaterials

Lucia M. Korpas, Rui Yin, Hiromi Yasuda, Jordan R. Raney

September 23, 2021

1 Fabrication of temperature-responsive multistable metamaterials

LCE preparation: The liquid crystal monomer, 1,4-bis-[4-(6-acryloyloxyhexyloxy)benzoyloxy]-2-methylbenzene (RM82) (Wilshire Technologies, Inc.), was melted at 130°C, then mixed in a 20 mL glass vial at 75°C with the chain extender, n-butylamine (Sigma-Aldrich) with a molar ratio of 1:1; 2 wt% of the photoinitiator, 2,2-Dimethoxy-2-phenylacetophenone (DMPA, Sigma-Aldrich); and 0.2 wt% of the inhibitor, butylated hydroxytoluene (BHT, Sigma-Aldrich). After stirring vigorously for 15 minutes, the materials were held at 75°C to oligomerize through a Michael addition reaction for 15 hours.

3D printing of LCE: The LCE ink was transferred into an opaque syringe and loaded into a custom pneumatic-controlled direct ink write (DIW) printer (modified from MakerGear) and preheated to the printing temperature of 75°C. This temperature was held for 30 minutes to allow equilibration. The LCE oligomers tend to align during extrusion due to shear in the nozzle, producing an anisotropic arrangement in the printed material. After printing the materials were cured via UV (Omnicure, S2000). Each set of prints (6 squares) was exposed to UV for 2 minutes immediately after printing. Subsequently, the whole batch of squares was further cured for 30 minutes after printing, with an intensity of 31 mW cm⁻².

PDMS preparation and printing: A PDMS formulation with a weight ratio of 87:13 SE-1700 to Sylgard 184 (Dow Corning) was mixed (FlackTek SpeedMixer). Materials were then loaded into a syringe and centrifuged to remove air bubbles. The PDMS portion of the hinges were subsequently printed using the DIW printer at room temperature.

Unit and chain assembly: Printed separately, the LCE and PDMS hinge layers were adhered using a thin layer of silicone glue. The squares were prepared by molding silicone (DragonSkin 10-SLOW, Smooth-On) in custom 3D-printed molds, designed to leave space for magnet and hinge insertion after curing. The hinges were then placed in and bonded to the squares with silicone. To provide an axial constraint (for load-displacement testing) and to reduce friction (for characterization of 1D chains of units), custom inserts were 3D printed (Vida HD, EnvisionTec) and removably placed at the center of each square, together with a cylindrical neodymium magnet (SuperMagnetMan).

2 Materials characterization

LCE and PDMS rheology: The rheological properties of the materials were characterized using a Discovery HR-3 Hybrid Rheometer (TA Instruments) with a 1° 40 mm cone plate geometry and a 500 μm gap (Fig. S1). The LCE ink was heated to 100°C to release the internal stress before testing. For each temperature, the LCE ink was equilibrated for 5 minutes. The shear stress was swept from 0.01 to 100 Pa at 1 Hz for the oscillatory measurements (Fig. S1(a)). The shear rate was swept from 0.01 to 100 s⁻¹ for the viscometry measurements (Fig. S1(b)).

LCE strain: LCE strain was measured as a function of temperature, $\epsilon_R(T)$, using single-layer printed samples (10 mm by 23 mm, with alignment along the major axis) suspended in an oven (Heratherm, Thermo Fischer). At each temperature setpoint a photograph was taken to record the change in length. The sample

lengths at each setpoint were determined using ImageJ analysis. Results are shown in Fig. 2(b) in the main text.

LCE phase transition: Differential scanning calorimetry (DSC) tests were performed on a TA Instruments Q2000. The 3D printable LCE ink was put into aluminum pans and heated and cooled at a ramping rate of 5°C per minute for two cycles from -40°C to 120°C. Results show a clear nematic-to-isotropic phase transition with a temperature peak of approximately 85°C (Fig. S4).

LCE alignment: Director alignment during printing was confirmed by polarized optical microscopy (POM). The POM images, shown in Fig. S3 were using an Olympus BX61. The brightness difference of the LCE film when the polarizers were placed at 45° and 90° indicate that the LCEs aligned well along the printing direction.

LCE and PDMS modulus: The dynamic thermomechanical properties of the materials after curing were obtained by dynamic mechanical analysis (DMA), using a TA Instruments RSA3 dynamic mechanical analyzer. The dimensions of the 3D printed LCE and PDMS samples were 35 mm × 6 mm (one layer). The samples were oscillated at 1 Hz to 0.02% strain. The temperature was ramped from 25°C to 140°C at a ramp rate of 5°C per minute. DMA results for the LCE are shown in Fig. 2a in the main text, and for PDMS in Fig. S5.

3 Experimental characterization of the metamaterial

Bilayer curvature: Bilayer hinge curvature $\kappa(T)$ was determined by photographing the curvature at each temperature setpoint, with hinges placed on a glass plate in an oven (Heratherm, Thermo Fischer) to control temperature. The changes in curvature were determined using the Fiji distribution of ImageJ [Schindelin2012] with the three-point circle plugin [Mason2017].

θ_T measurement: Temperature-induced angle $\theta_T(T)$ was measured by placing unit cell samples in a custom thermally-insulated box (with temperature controlled by a heat gun); samples rested on a glass surface with low-friction contact points where they equilibrated for 20 minutes at each temperature setpoint (with experimental uncertainty of $\pm 2^\circ\text{C}$), after which they were photographed. The changes in angle were determined from the photographs using the Fiji distribution of ImageJ.

Load-displacement relation: The load-displacement relationships for unit cells were determined using a custom-made materials tester (load cell LUX-B-50N-ID, KYOWA), with a custom fixture providing a vertical constraint on the centers of the squares while allowing free rotation and horizontal translation. Temperature control was provided by loading the samples within a custom-made thermally-insulated box heated by a heat gun (Fig. S6). Samples were equilibrated for 20 minutes at each temperature setpoint, after which a test was conducted from a strain of -0.05 to 0.30 at 1 mm/s.

Metamaterial chain demonstrations: During all tests, chains were placed on a precision-ground surface coated with a low-friction layer (ultra high molecular weight polyethylene, McMaster) with low-friction inserts as the contact points between the chain and the surface. *Free boundary:* With the chain unconstrained, a heat gun was held within ~ 10 cm of the chain at different points along the chain. The position was fixed for the duration of each test and time was allowed for the chain to cool between tests. *Length constraint:* a constraint preventing motion along the chain axis, but allowing free rotation and translation perpendicular to the chain axis, was applied to the squares at the ends of the chain. Local changes in temperature were applied as described for the free-boundary case. *Actuation:* Directional “feet” were fixed to the bottom of each square, replacing the original low-friction inserts (Fig. S2). Silicone pneumatic tubing was fixed to the top of the squares, running partially along the length of the chain, and pressure was applied cyclically using a pressure controller (Nordson EFD).

4 Numerical modeling

The potential energy for the rotating squares mechanism depends on the torsional energy of the hinges and the potential energy of the embedded magnets. The analysis of the hinges (with thickness h , LCE thickness ratio r) is approximated empirically by Euler-Bernoulli beam theory. The position of the neutral axis h_0

relative to the LCE surface is

$$h_0(T) = \frac{\frac{1}{2}E_{\text{PDMS}}h_{\text{PDMS}}^2 + \frac{1}{2}E_{\text{LCE}}(T)h_{\text{LCE}}^2 + E_{\text{PDMS}}h_{\text{PDMS}}h_{\text{LCE}}}{E_{\text{PDMS}}h_{\text{PDMS}} + E_{\text{LCE}}(T)h_{\text{LCE}}} \quad (1)$$

with elastic moduli E_{PDMS} and $E_{\text{LCE}}(T)$ and thicknesses $h_{\text{PDMS}} = (1 - r)h$ and $h_{\text{LCE}} = rh$ of the PDMS and LCE layers, respectively. Assuming rectangular cross sections with width w , the equivalent linear hinge stiffness is thus

$$k_{\text{H}}(T) = \frac{E_{\text{PDMS}} \left[I_{\text{PDMS}} + wh_{\text{PDMS}} \left(h - h_0(T) - \frac{h_{\text{PDMS}}}{2} \right)^2 \right] + E_{\text{LCE}}(T) \left[I_{\text{LCE}} + wh_{\text{LCE}} \left(h_0(T) - \frac{h_{\text{LCE}}}{2} \right)^2 \right]}{s} \quad (2)$$

with second moments of area $I_x = \frac{wh^3}{12}$ for $x = \text{LCE}, \text{PDMS}$ and arc (beam) length $s = bh^2$, with b determined empirically (see Fig. S8). In practice, the squares will deform to some degree during hinge rotation. We account for this by adding a torsional spring k_{S} , which is temperature-independent and has constant value across samples, in series with the temperature-dependent k_{H} , for an effective torsional stiffness

$$k(T) = (1/k_{\text{H}}(T) + 1/k_{\text{S}})^{-1} \quad (3)$$

We empirically select $k_{\text{S}} = 0.0050 \text{ Nm}$ and use this bending stiffness to model the hinge as a linear torsional spring with stiffness k and initial folding angle $\theta_{\text{L}} + \theta_{\text{T}}(T)$, where θ_{L} is a fabrication parameter and $\theta_{\text{T}}(T)$ is the change in this as a result of the bilayer bending. This gives the strain energy function

$$U_{\text{H}}(\theta, T) = \frac{1}{2}k(T)[\theta - (\theta_{\text{L}} + \theta_{\text{T}}(T))]^2 \quad (4)$$

To model $\theta_{\text{T}}(T)$ we use a modified version of Timoshenko's bimetallic strip theory for curvature $\kappa(T)$, where, in place of a constant thermal expansion coefficient, an empirically-determined strain-temperature relation $\varepsilon(T)$ is used:

$$\kappa(T) = \left(\frac{1}{h} \right) \frac{\varepsilon(T)}{\frac{1}{2} + \frac{w}{6}[E_{\text{LCE}}(T)r^3 + E_{\text{PDMS}}(1 - r)^3] \left[\frac{1}{E_{\text{LCE}}(T)r} + \frac{1}{E_{\text{PDMS}}[1-r]hw} \right]} \quad (5)$$

From this, we relate the curvature to the resulting angle by the arc length as $\theta_{\text{T}}(T) = \kappa(T)s$.

The magnetic contributions, restricted to nearest-neighbor pairwise interactions, were modeled by point dipoles of magnetic moment m at the centers of the adjacent squares with alternating polarity. In the rigid-folding limit, the displacement d of the centers of adjacent squares is prescribed by the rotation θ of adjacent squares as $d(\theta) = 2L \cos \theta$, where L is half the square's diagonal, from center to vertex. From this, the magnetic potential of adjacent magnets (which attract one another) is given by

$$U_{\text{M}}(\theta) = -\frac{\mu_0 m^2}{2\pi d(\theta)^3} \quad (6)$$

with μ_0 being the magnetic permeability of free space. We find that an empirical value of $m = 0.1778 \text{ NA}^2$ accounts for the insertion of the magnets and for their moment, based on the experimental points in Fig. 5(a-c). At large θ adjacent squares begin to come into contact and deform. This was modeled as

$$U_{\text{limit}}(\theta) = A(e^{B\theta} + e^{-B\theta} - 2) \quad (7)$$

with empirical values $A = 1e^{-14}$ and $B = 30$. The total strain energy for a pair of squares is then

$$U(\theta, T) = U_{\text{H}}(\theta, T) + U_{\text{M}}(\theta) + U_{\text{limit}}(\theta) \quad (8)$$

To determine the empirical parameters from force-displacement data at a given temperature, the force-angle relation for two pairs of squares is derived from $U(\theta, T)$:

$$F(\theta, T) = 4 \left[\frac{M_{\text{H}}(\theta, T) + M_{\text{M}}(\theta) + M_{\text{limit}}(\theta)}{2L \cos(\theta)} \right] \quad (9)$$

with

$$\begin{aligned} M_{\text{H}}(\theta, T) &= -2k(T)\theta \\ M_{\text{M}}(\theta) &= \frac{3\mu_0 m^2 L \sin \theta}{2\pi d(\theta)^4} \\ M_{\text{limit}}(\theta) &= -AB(e^{B\theta} - e^{-B\theta}) \end{aligned} \tag{10}$$

The relation $d(\theta)$ is used to convert between the measured displacement and the theoretical angle at this displacement.

5 Figures

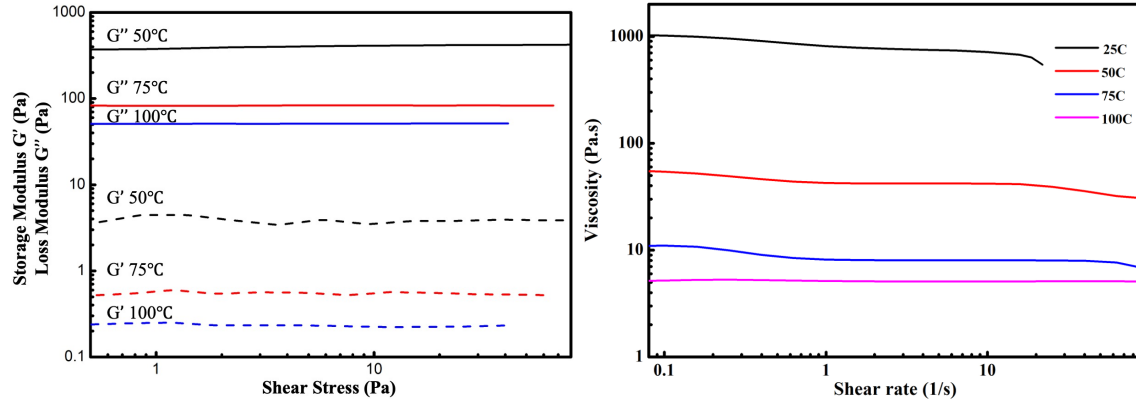


Figure S1: LCE ink rheological properties before UV curing. (a) LCE storage modulus (dashed line) and loss modulus (solid line) are independent of shear stress in the printing regime. (b) LCE ink viscosity decreases with increased temperature, dropping more than two orders of magnitude upon heating from room temperature to 100°C.

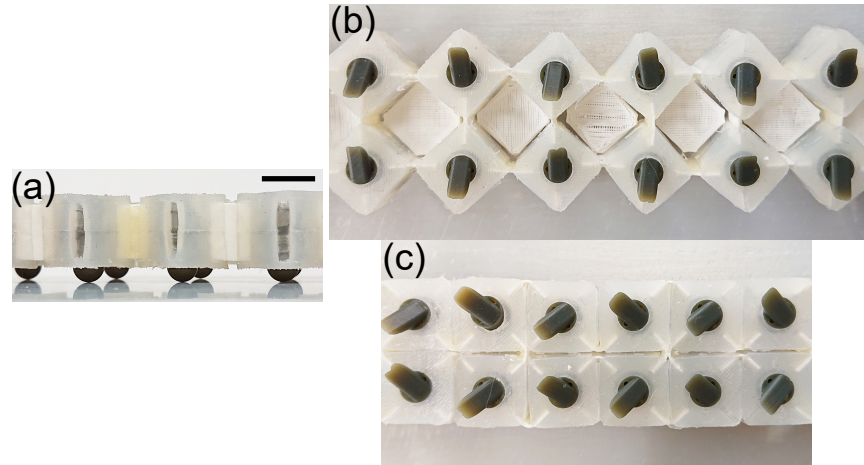


Figure S2: Inserts used in chains: (a) rounded contact point for lowering friction, and (b-c) angled “feet” to enable change in traction with phase transformation, with the same sample shown in the open (b) and closed (c) configuration.

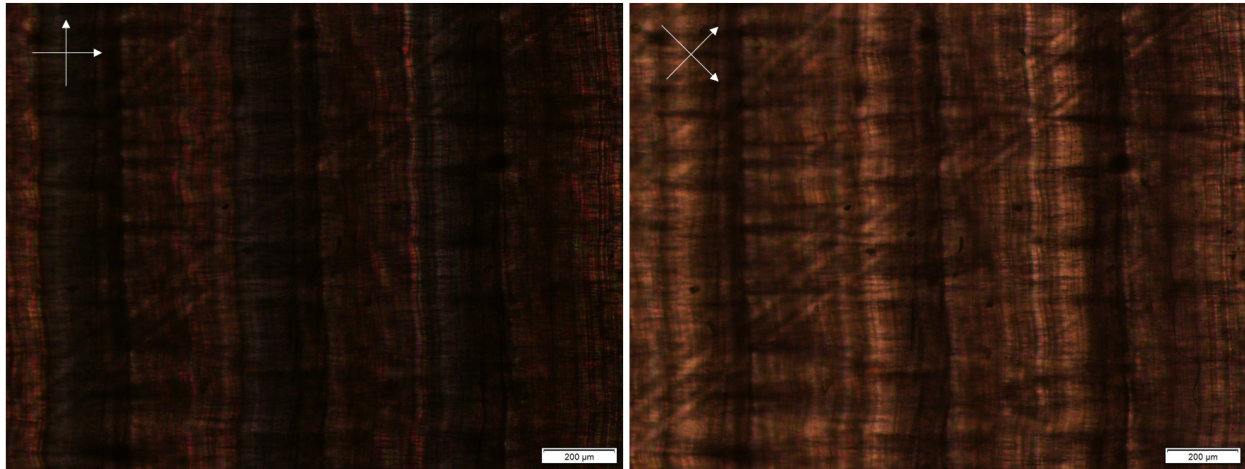


Figure S3: Polarized optical microscopy (POM) images of an LCE film, with polarizers placed at 90° (left) and 45° (right). The brightness difference is a qualitative indication of LCE alignment.

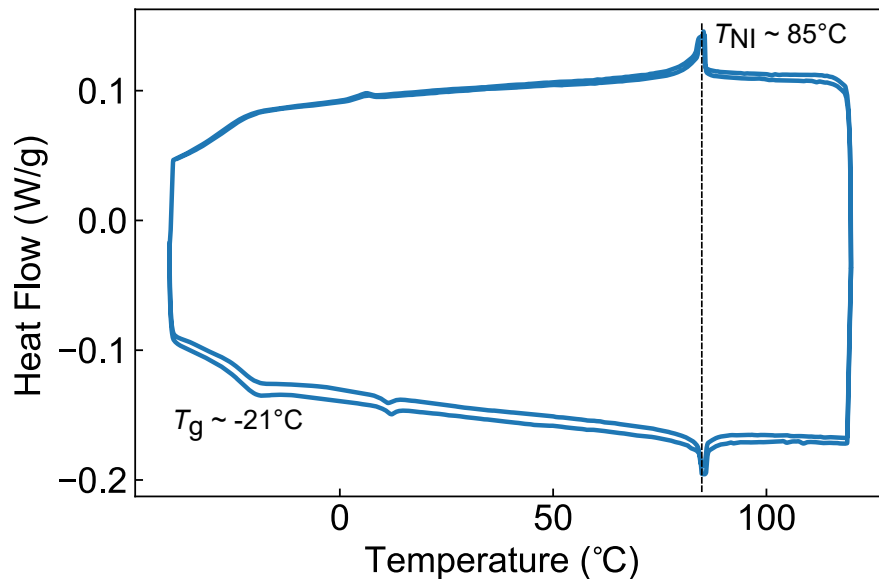


Figure S4: Differential scanning calorimetry (DSC) of LCE ink. The nematic-to-isotropic phase transition temperature peak is clearly shown at 85°C . The LCE ink was printed at 75°C to ensure it remained below this temperature, within the nematic phase, during printing.

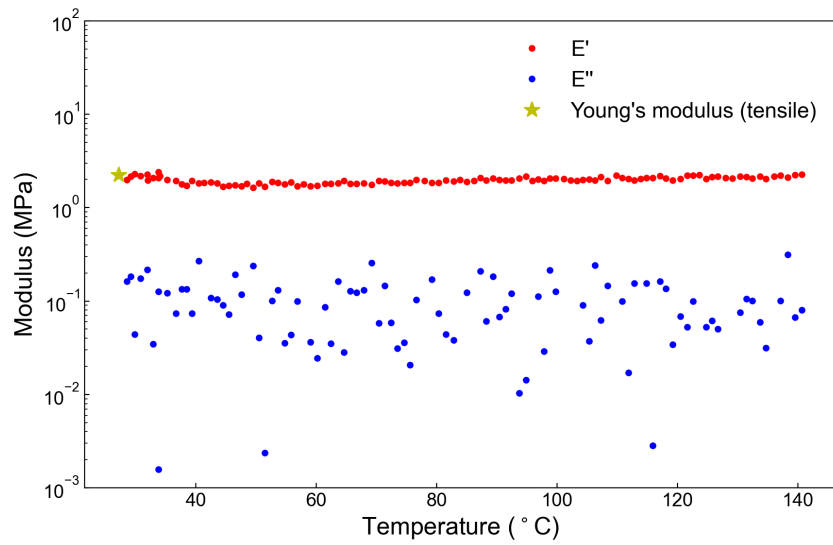


Figure S5: Tensile storage and loss moduli of the cured PDMS are nearly independent of temperature in the range of interest.

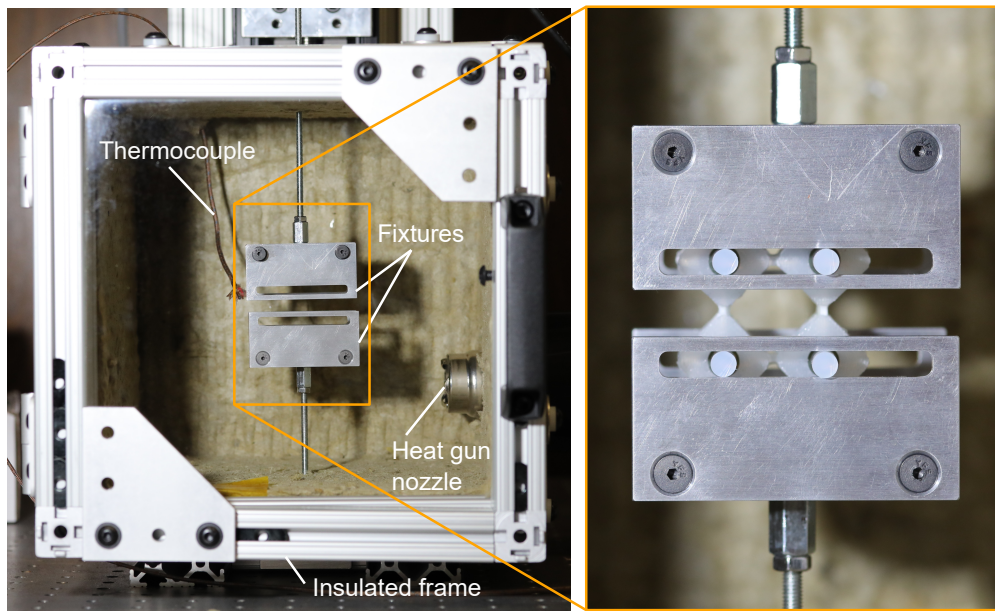


Figure S6: Annotated photo of insulated enclosure. This enclosure provides a uniform elevated temperature around a sample as its surrounding area is heated with a heat gun; the temperature was monitored using the thermocouple. The enclosure was used in load-displacement testing (using the fixture shown in the callout) and measurement of θ_T (without the fixture).

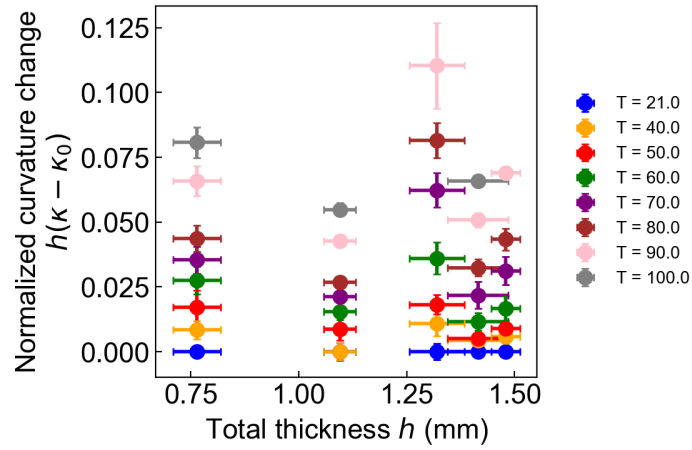


Figure S7: Normalized change in curvature does not depend on h .

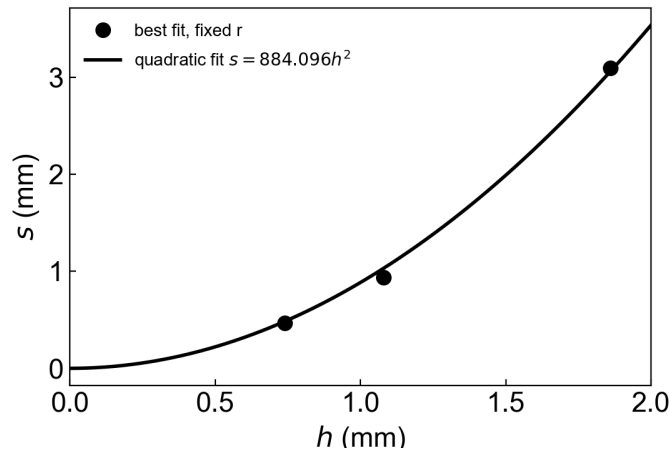


Figure S8: Empirical model for effective (best-fit) arc length s as a function of h . Used quadratic fit $s = bh^2$ instead of linear to avoid a singularity that occurs for an x-intercept > 0 .

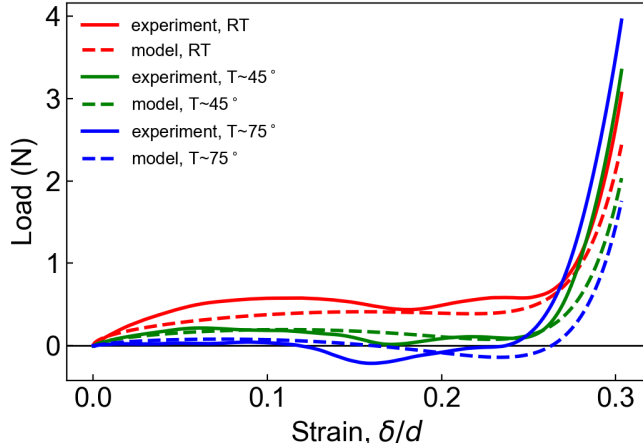


Figure S9: Force-displacement data for $(h, r) = (1.71 \text{ mm}, 0.18)$, with magnets included, at three temperatures, showing experimental (solid line) and modeled (dashed line) curves.

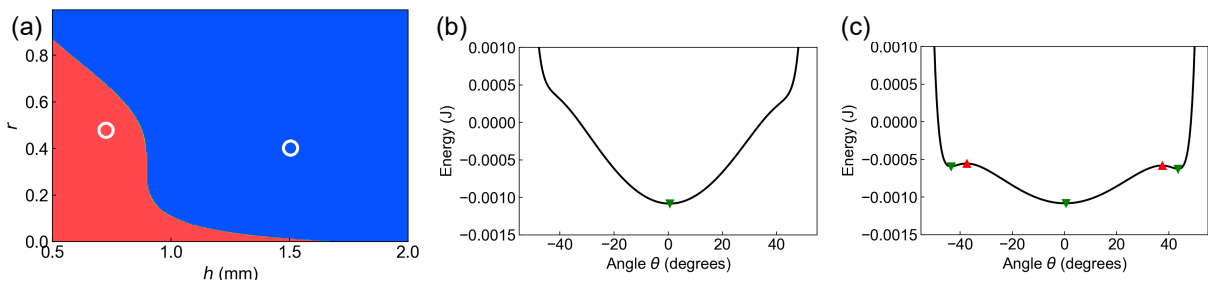


Figure S10: Stability of chains used in demonstration Figs. 6 and 7. (a) By choosing the two design parameter values shown here we can experimentally demonstrate that the resulting chains were in the stability regimes expected by the model. (b-c) Energy landscapes for (b) $(h, r) = (1.50 \text{ mm}, 0.40)$ and (c) $(h, r) = (0.73 \text{ mm}, 0.47)$ showing mono- and tristability, respectively.